Single-Shot Spiral Imaging Enabled by an Expanded Encoding Model: Demonstration in Diffusion MRI

Bertram J. Wilm,[1]* Christoph Barmet,[1,2] Simon Gross,[1] Lars Kasper,[1,3] S. Johanna Vannesjo,[1] Max Haeberlin,[1] Benjamin E. Dietrich,[1] David O. Brunner,[1] Thomas Schmid,[1] and Klaas P. Pruessmann [1]

Purpose: The purpose of this work was to improve the quality of single-shot spiral MRI and demonstrate its application for diffusion-weighted imaging.

Methods: Image formation is based on an expanded encoding model that accounts for dynamic magnetic fields up to third order in space, nonuniform static B_0, and coil sensitivity encoding. The encoding model is determined by B_0 mapping, sensitivity mapping, and concurrent field monitoring. Reconstruction is performed by iterative inversion of the expanded signal equations.

Diffusion-tensor imaging with single-shot spiral readouts is performed in a phantom and in vivo, using a clinical 3T instrument. Image quality is assessed in terms of artefact levels, image congruence, and the influence of the different encoding factors.

Results: Using the full encoding model, diffusion-weighted single-shot spiral imaging of high quality is accomplished both in vitro and in vivo. Accounting for actual field dynamics, including higher orders, is found to be critical to suppress blurring, aliasing, and distortion. Enhanced image congruence permitted data fusion and diffusion tensor analysis without coregistration.

Conclusion: Use of an expanded signal model largely overcomes the traditional vulnerability of spiral imaging with long readouts. It renders single-shot spirals competitive with echo-planar readouts and thus deploys shorter echo times and superior readout efficiency for diffusion imaging and further prospective applications. **Magn Reson Med 77:83–91, 2017.**

Key words: single-shot spiral; algebraic image reconstruction; magnetic field monitoring; magnetic field probes; DWI; DTI

INTRODUCTION

Spiral k-space sampling (1) holds great potential for many MRI applications attributed to a number of favorable properties (2–4). Spiral trajectories are among the fastest ways of encoding a given resolution and field of view (FOV). They give rise to approximately isotropic point-spread functions and are readily amenable to navigator and variable-density sampling approaches. Center-out spirals also exhibit inherently short echo times, which often benefit the signal-to-noise ratio yield.

Spiral readouts are particularly attractive for single-shot acquisition. Single-shot imaging provides robustness against motion-related artifacts, which further improves with short echo times. It also offers high efficiency of spatial encoding, which is most valuable after extensive signal preparation, such as in blood-oxygen-level–dependent functional MRI or diffusion-weighted (DW) imaging (DWI). Despite these benefits, single-shot spiral readouts have rarely been demonstrated and are virtually not used in practice to date. This is attributed mainly to their sensitivity to B_0 off-resonance and gradient imperfections.

The dominant sources of B_0 off-resonance are susceptibility differences within the subject and relative to surrounding material and air. Slow variation of B_0 that is effectively static over a readout can also be caused by breathing motion or magnet drifts. In common spiral scans, B_0 off-resonance results in broadened or ring-shaped point-spread functions. In images, they are manifest chiefly as blurring, yet may also appear as ringing, signal cancelations, and distortion.

One effective way of diminishing off-resonance effects is to reduce the duration of individual spiral readouts. This can be achieved by multiple-shot approaches (5–7), which have proven particularly useful for diffusion imaging. Multiple-shot imaging is challenging, however, in that it requires data to be consistent across interleaves, which may not be the case in the presence of motion or changes in the behavior of the gradient system. Staying with single-shot acquisition, readouts can also be shortened by parallel imaging (8–11). However, the achievable degree of acceleration is limited such that off-resonance often remains a problem in single-shot MRI.

Another way of addressing B_0 nonuniformity is to include it in the signal model and remediating it at the image reconstruction stage (12). Among others, B_0 correction for non-Cartesian sampling has been approached from an inverse-problem perspective, deploying conjugate-

[1]Institute for Biomedical Engineering, University of Zurich and ETH Zurich, Zurich, Switzerland.

[2]Skope Magnetic Resonance Technologies Inc, Zurich, Switzerland.

[3]Translational Neuromodeling Unit, Institute for Biomedical Engineering, University of Zurich and ETH Zurich, Zurich, Switzerland.

*Correspondence to: Bertram J. Wilm, Institute for Biomedical Engineering, University and ETH Zurich, Gloriastrasse 35, CH-8092 Zurich, Switzerland. E-mail: wilm@biomed.ee.ethz.ch

Klaas Pruessmann holds a research agreement and receives research support from Philips Healthcare. He is a shareholder of Gyrotools LLC and Skope Magnetic Resonance Technologies Inc. Bertram Wilm, Christoph Barmet, and David Brunner are associates and shareholders of Skope Magnetic Resonance Technologies Inc.

Received 27 May 2016; revised 29 August 2016; accepted 14 September 2016

DOI 10.1002/mrm.26493

Published online 21 October 2016 in Wiley Online Library (wileyonlinelibrary.com).

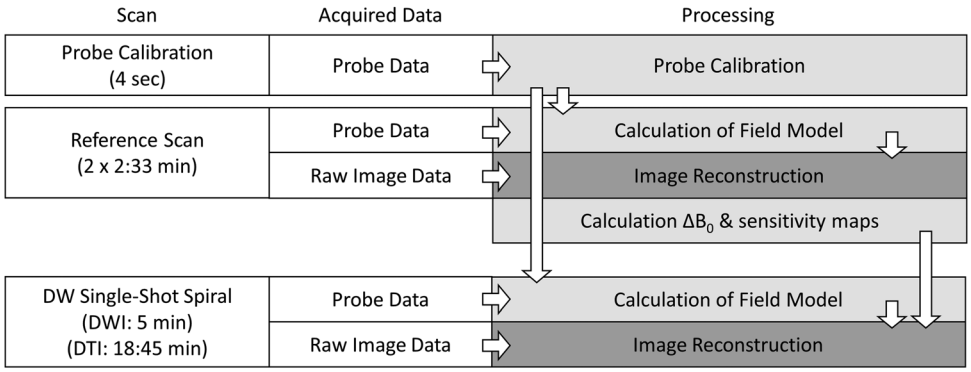

FIG. 1. Overview of data acquisition and processing steps.

gradient solvers for the cases of full Fourier encoding (13) and parallel imaging (14). B_0-correcting image reconstruction is computationally demanding, but practical with modern computing infrastructure. However, perturbation of Fourier encoding by B_0 nonuniformity tends to worsen the conditioning of the inverse problem and thus to boost the propagation of model errors into resulting images. B_0-correcting reconstruction thus requires highly accurate knowledge not only of the static ΔB_0, but also of gradient and other field dynamics, and of receiver coil sensitivity, if applicable.

Relevant imperfections of field dynamics include the low-pass behavior of gradient chains, anisotropic gradient delays (15), eddy currents (16,17), mechanical (18) and thermal (19,20) behavior of gradient coils, gradient cross-terms (21), concomitant fields (22), and magnet drifts. Unlike echo-planar imaging (EPI), spiral scanning does not lend itself to calibration based on repetitive features of gradient waveforms (23). Instead, actual spiral trajectories are typically obtained by k-space mapping (24–29). However, separate trajectory measurement does not capture field drift and variation of field dynamics during extended scans. More-comprehensive field information is retrieved by concurrent measurement with nuclear magnetic resonance (NMR) field probes (27,30), which also permit recording field dynamics of second and higher order in space (31).

The goal of the present work is hence to explore single-shot spiral imaging based on an expanded signal model fed by static off-resonance maps, concurrent field monitoring, and coil sensitivity information. Spiral acquisition is deployed for DWI, which is prone to field imperfections (32), yet would benefit particularly from reduced echo times and enhanced robustness against motion.

METHODS

Overview and Encoding Model

In this work, MR imaging encoding is described by the following signal model (Eq. 1):

$$\sigma_\gamma(t) = \int \rho(\boldsymbol{r})\ s_\gamma(\boldsymbol{r}) e^{-i[\sum_l k_l(t) b_l(\boldsymbol{r})] - i\Delta\omega(\boldsymbol{r})t} d\boldsymbol{r} \qquad [1]$$

where $\sigma_\gamma(t)$ denotes the NMR signal that is acquired by the γ-th receive coil at time point t. $\rho(\boldsymbol{r})$ describes the transverse magnetization as a function of the spatial coordinate $\boldsymbol{r}$. The receive sensitivity of coil γ is denoted by $s_\gamma(\boldsymbol{r})$, i denotes the imaginary unit $\sqrt{-1}$, and l counts the phase coefficients $k_l(t)$ that describe the magnetic field dynamics. Following the conventional k-space formalism, every phase coefficient $k_l(t)$ is related to a spatial basis function $b_l(\boldsymbol{r})$ (27,31). The resonance offset due to static field inhomogeneity ΔB_0 at position $\boldsymbol{r}$ is denoted by $\Delta\omega(\boldsymbol{r})$.

The phase coefficients $k_l(t)$ were obtained by concurrent field monitoring. Importantly, field monitoring was performed both during spiral scans and during reference scans for mapping s_γ and $\Delta\omega$. As a consequence, all image-domain data are represented in the coordinates induced by the gradient system and is thus spatially congruent. Back-to-back calibration of the field probes and acquisition of ΔB_0 maps ensured automatic accounting for subsequent field drifts.

Hardware Setup, Phantoms, and Subjects

Imaging was performed on a 3 Tesla Achieva System (Philips Healthcare, Best, The Netherlands) using an eight-element head coil array. Sixteen transmit-receive ^{19}F-based NMR (27,30) field probes were mounted on the head coil (32). The T_2 of the field probes was approximately 50 ms. A minimum repetition time (TR) of 150 ms was used to avoid significant perturbation by echoes during the probe readouts. Subsequent to probe excitation, NMR signals from the field probes were acquired through the MR scanner spectrometer synchronously with the imaging data.

The in vitro experiments were performed using a spherical phantom of 20-cm diameter, filled with extremely low-diffusive silicon oil (AK 500; Wacker Chemie AG, Munich, Germany) to minimize diffusion-induced signal attenuation. In vivo imaging was performed on 2 healthy subjects.

MR Sequences

Figure 1 illustrates the data acquisition and processing steps, which are described in more detail in this and the following subsection.

Before the imaging experiments, the field probes' position and off-resonance were calibrated (27).

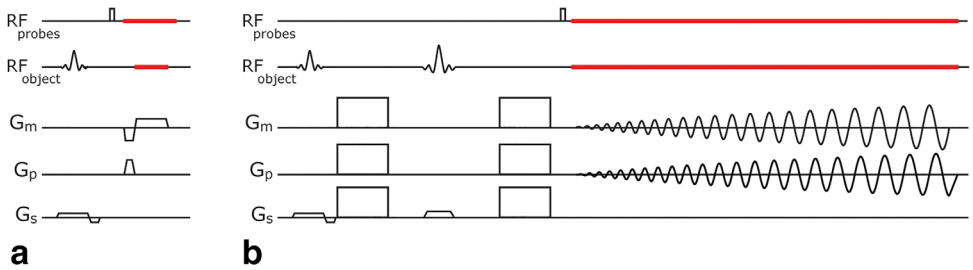

FIG. 2. Sequence schematics. For the gradient echo sequences, NMR field probes are excited before phase encoding (3). In the single-shot spiral images, the probe field evolution is recorded (red) after the diffusion-sensitizing gradients.

As an input to coil sensitivity and static ΔB_0 map calculation, standard spin-warp gradient-echo sequences (Fig. 2a) with an echo time (TE) of 2.4 and 2.9 ms were performed in a transverse plane (resolution = $(1.3\,\text{mm})^2$; FOV = $(230\,\text{mm})^2$; slice thickness = 4 mm; TR = 1 second). For field monitoring, the probes were excited directly after the slice rephasing gradient (Fig. 2a).

For the same geometry, single-shot DW spin-echo spiral scans were acquired using a Stejskal-Tanner diffusion sequence (Fig. 2b), with diffusion weighting applied in 24 directions (b = 1,000 s/mm^2; resolution = $(1.3\,\text{mm})^2$; slice thickness = 2 mm; TR = 5 seconds). In addition, a b0 (b = 0) image was acquired to obtain a complete diffusion tensor imaging (DTI) data set. For field monitoring, the field probes were excited after the second diffusion-sensitizing gradient (Fig. 2b) to avoid dephasing by the diffusion-weighting gradients and to limit T_2^* decay of the field probe signal. To add some structure to the phantom, two saturation slabs were applied in the phantom experiments. The gradient system was operated at a gradient strength of 80 mT/m and with a slew of 100 mT/m/ms to minimize the echo time, achieving a TE of only 34 ms. To mitigate static B_0 off-resonance effects, the k-space undersampling factor was chosen to be 4, which resulted in an acquisition duration of 32 ms. This was implemented as an interleaved spiral sequence with four interleaves, each of them being separately reconstructed as a single-shot acquisition.

In the phantom scans, the number of repetitions (of each interleave) was four. To demonstrate the image quality for different static ΔB_0 situations in vivo, three slices of a healthy male subject were acquired using four repetitions. To demonstrate a high-resolution DTI evaluation, one slice was acquired with 15 repetitions of each interleave. The total acquisition time was 5:00 and 18:45 minutes per slice respectively. Note that because of limitations in data streaming of the synchronous ^{1}H and ^{19}F signal acquisition, a long sequence repetition time of 5 seconds had to be chosen. Therefore, the DW sequence was performed only for a few slices. An improved implementation of the scanner's acquisition software should allow for full multislice capability.

Data Processing and Image Reconstruction

The dynamic field evolution, as described by the k-space coefficients $k_l(t)$, was calculated for each scan (27). As spatial basis functions $b_l(r)$, real-valued spherical harmonics up to the third order (31) and the second-order concomitant field basis functions (22) were used. In order to interpret and compare field coefficients relating to basis functions of different spatial orders—having units of rad, rad/m, rad/m^2 and rad/m^3, respectively—the maximum field excursion in a centered sphere of 20-cm diameter was calculated for all higher-order phase coefficients (31) and denoted by rad_{max}.

Image reconstruction was performed using higher-order iterative sensitivity encoding (SENSE) reconstruction (31). In a first step, the spin-warp gradient echo images were reconstructed based on Equation 1, using the measured coefficients $k_l(t)$ without the incorporation of $s_\gamma(\boldsymbol{r})$ and $\Delta\omega(\boldsymbol{r})$ terms. From these images, receive coil sensitivities $s_\gamma(\boldsymbol{r})$ and $\Delta\omega(\boldsymbol{r})$ off-resonance maps were calculated. Subsequently, the DW data were reconstructed using the measured coefficients $k_l(t)$ as well as the sensitivity maps $s_\gamma(\boldsymbol{r})$ and the off-resonance map $\Delta\omega(\boldsymbol{r})$ for static ΔB_0 off-resonance correction. For the gradient echo data, image reconstruction was performed using five iterations. For the single-shot DW spiral data, 35 iterations were used for each image average. The final DW images were calculated by a sum-of-squares combination of all image averages.

Specific Image Reconstructions

To assess the influence of the applied dynamic encoding model, the DW in vitro data were reconstructed multiple times with varying encoding models using the iterative SENSE algorithm:

- First, on the basis of the nominal (first-order) *k*-coefficients, calculated from the nominally applied field gradients, to demonstrate reconstruction results based on nominal encoding.
- Second, using a first-order field model (including k_0) as monitored during the b0 scan, but omitting the second- and third-order *k*-coefficients; in this way, the exclusion of eddy currents induced by the DW gradients is simulated.
- Finally, image reconstruction was performed based on the concurrently monitored full third-order *k*-coefficients.

All reconstructions of the DW in vitro data included static ΔB_0 off-resonance correction.

To assess how well the geometry of the reconstructed DW images matches, a relative difference image between one DW image and the b_0 image was calculated. The relative difference between two magnitude images I_1 and I_2

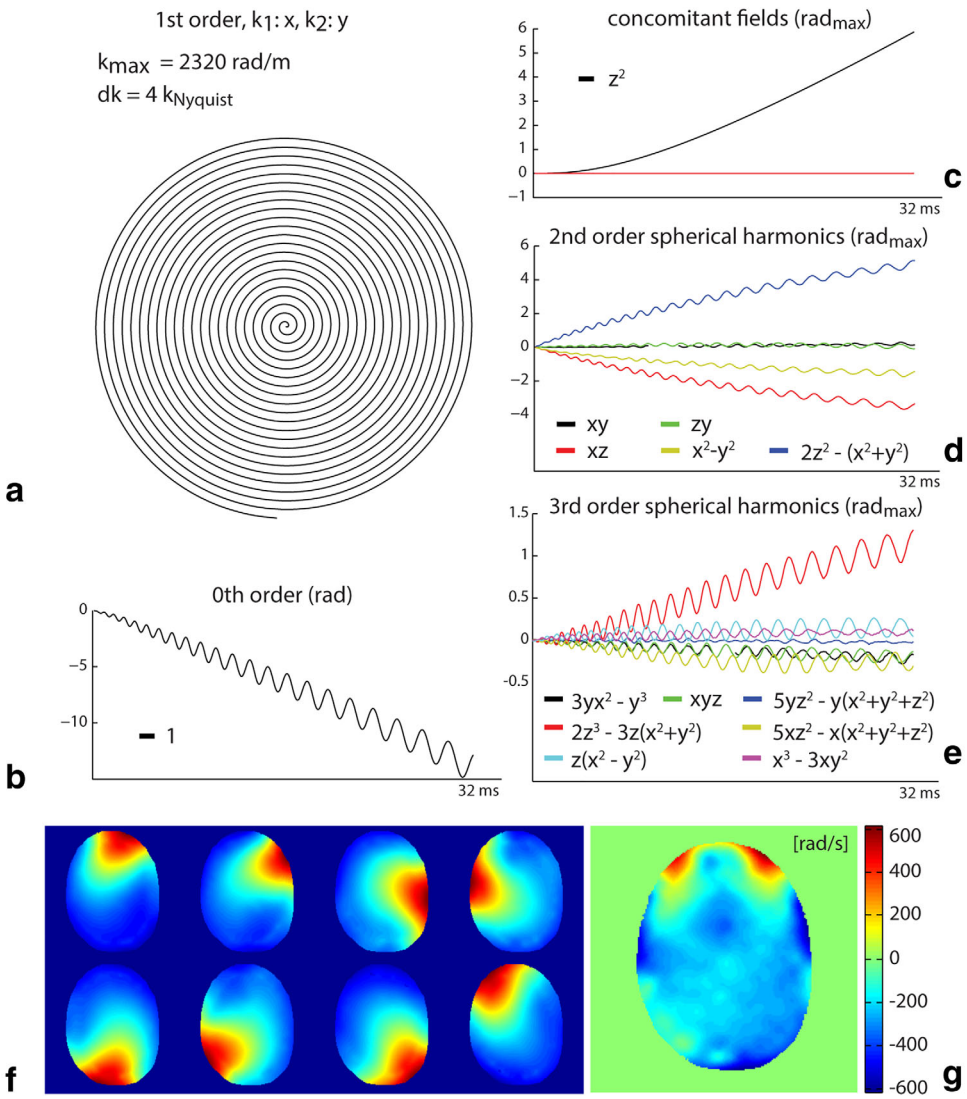

FIG. 3. Input data to the encoding model. (a–e) Monitored dynamic encoding fields over the time of the readout (32 ms); first-order k-space coefficients (read gradients) (a), zero-order phase (b); higher-order dynamic field effects (c–e) are scaled to show the maximum effect within the imaging volume in radians relating to each basis function. (f) Receive coil sensitives (relative values) for the eight coils. (g) Static off-resonance map.

was calculated as $(I_1\text{-}I_2)/(I_1/2+I_2/2)$. Given the extremely low diffusivity of the phantom liquid, these differences are expected to vanish.

The above-mentioned image reconstruction was also conducted for the in vivo data. Moreover, to assess the effect of static ΔB_0 off-resonance on image quality, the in vivo data were reconstructed

- with static ΔB_0 correction;
- without static ΔB_0 correction.

This was performed for the monitored first-order dynamic field model to evaluate the effect of ΔB_0 correction for the commonly performed first-order image reconstruction. The nominal reconstruction was performed without static ΔB_0 correction. The higher-order monitored reconstruction was performed with static ΔB_0 correction in order to demonstrate achievable image quality using the proposed encoding model on an in vivo data set.

To assess the effect of the utilized reconstruction models on quantitative diffusion imaging, the in vivo data were fitted to a diffusion tensor model (33), and the apparent diffusion coefficients and fractional anisotropy maps were calculated.

RESULTS

Figure 3 shows the recorded field evolution during one DW spiral acquisition. In addition to the first-order read gradients that are shown in parametric view (Fig 3a), zero-order field changes (Fig. 3b) with a maximum deviation of 15 rad during the readout as well as oscillatory terms are visible (zero to third order; Fig. 3). The dominating higher-order fields (Fig. 3c–e) originate from concomitant fields of the read gradients (Fig. 3c) with an effect of 6 rad_{max} as well as long-lived eddy current fields from the diffusion weighting gradients (Fig. 3d,e)

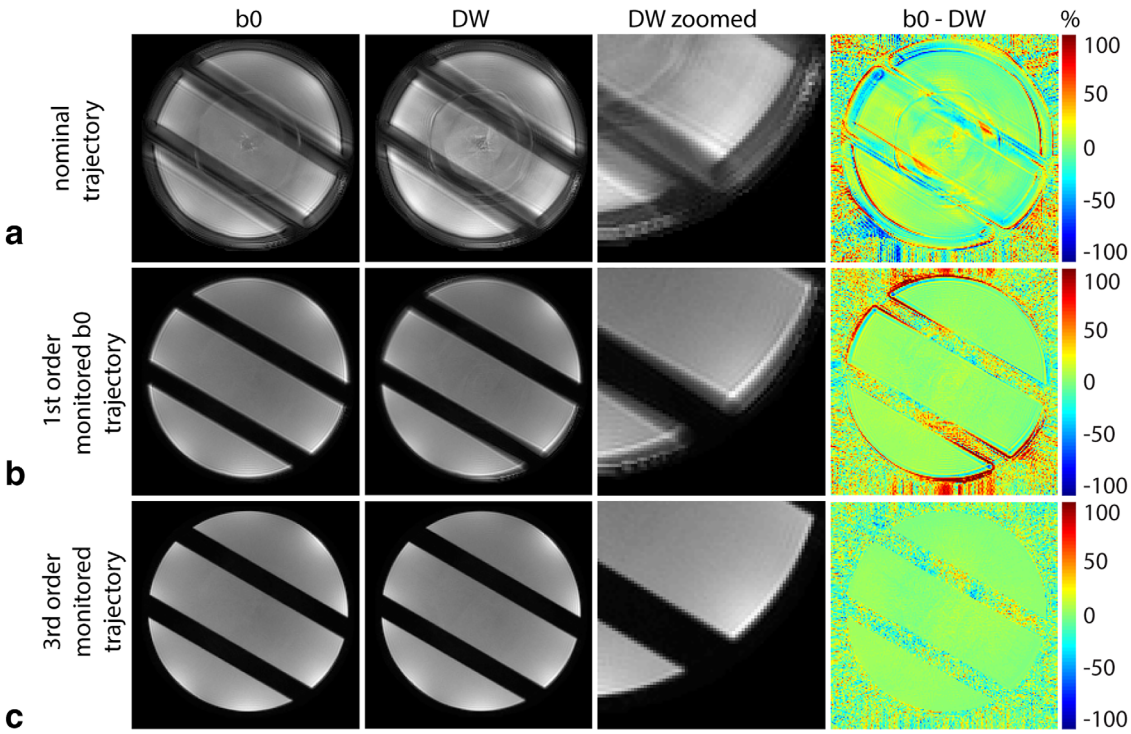

FIG. 4. Effect of the dynamic encoding model on the image quality and geometrical congruence. Images reconstructed using the nominal k-space trajectory (a), the monitored zero- and first-order encoding of the non-DW (b0) acquisition (b), and using the concurrently monitored higher-order field evolution (c). The blue arrows highlight an aliasing-like artifact; red arrows highlight blurring artifacts.

with an effect of up to 5 rad_{max}. The encoding of the b0 scan (data not shown) was very similar to the encoding in the DW acquisition, apart from the higher-order terms that were essentially absent, except for the concomitant field effect as has been previously observed for DW EPI (31).

Image reconstruction on the nominal trajectory resulted in strong blurring artifacts and intensity mismatch of the DW images (Fig. 4a). The incorporation of monitored zero- and first-order fields drastically improved the image quality of the b0 image (Fig. 4b). The DW images, however, still show remaining artifacts, leading to incongruence among the images of different DW directions (Fig. 4b), as indicated in the difference images. This can be explained by the fact that the higher-order spherical harmonic terms were present only in DW encoded images, and given that the data were acquired near to the isocenter in a nontilted axial plane, the contribution of the concomitant field terms was very minor.

Incorporating higher-order fields did remove the remaining image artifacts and strongly improved the geometrical congruence of the data set, as reflected by strongly diminished differences between b0 and DW image (Fig. 4, bottom).

The in vivo DW images (Fig. 5) that are reconstructed on the nominal trajectories (Fig. 5a) show strong blurring artifacts. Even without static ΔB_0 correction, these artifacts are significantly reduced when reconstructing on the monitored first-order b0 trajectory (Fig. 5b). The inclusion of static ΔB_0 correction (Fig. 5c) removes blurring artifacts, particularly in the lateral regions of the brain such as in the area of the frontal lobe (Fig. 5c, blue arrow). The incorporation of the dynamic higher-order terms further significantly improves the image quality. This is visible, for example, in the posterior region of the brain (Fig. 5c, red arrow), where blurring artifacts that are present in the first-order reconstructed images are removed. An animation of the reconstructed images that allows for best visual comparison of the different image reconstructions is available online in the Supporting (Video S1).

Slight residual blurring artifacts can be observed in the frontal lobe, where the static B_0 gradient is steep (Figs. 5d [blue arrow] and 6 [blue arrow]).

In the in vivo DTI data (Fig. 7), the nominally reconstructed images (Fig. 7a) show largely implausible diffusivity values, as is to be expected from the underlying b0 and DW images. Data quality greatly improved when using the DW images reconstructed on the concurrently monitored higher-order trajectory including static off-resonance correction. In this case, even fine anatomical details are visible, also in the region of the frontal lobes, a region where imaging is typically challenged by off-resonance artifacts.

DISCUSSION AND CONCLUSION

According to the results of this work, use of an expanded signal model in conjunction with model inversion for reconstruction facilitates the deployment of single-shot spiral readouts for DWI. The signal model used here comprised dynamic fields up to the third order in space, static B_0 off-resonance, and receive coil sensitivity.

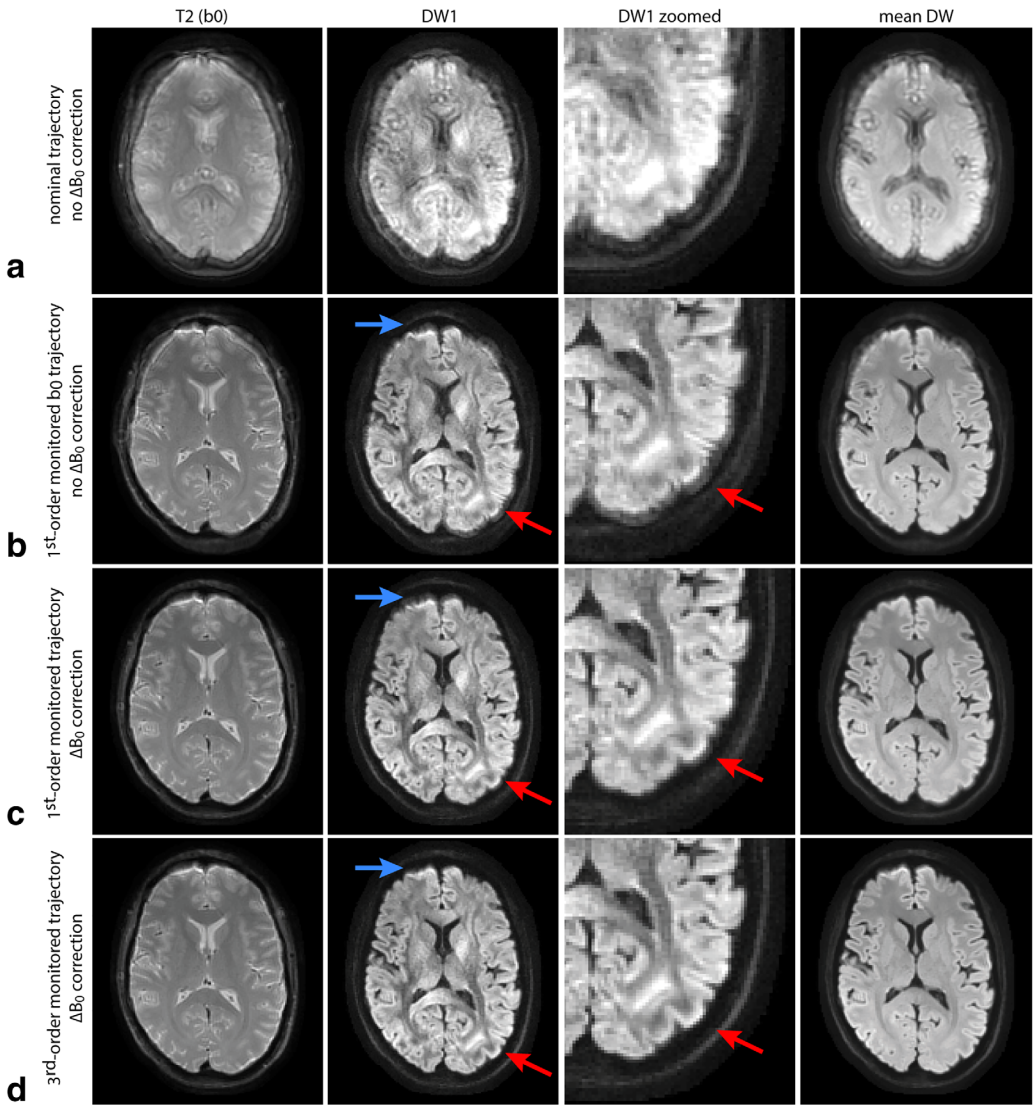

FIG. 5. In vivo single-shot spiral images. Columns (left to right): T2-weighted (b0) image, single DW image, mean DW image. Rows: Image reconstructed with (c,d) and without (a,b) static B_0 correction using the nominal k-space trajectory (a), the monitored zero- and first-order encoding of the non-DW (b0) acquisition (b,c), and using the concurrently monitored higher-order field evolution (d). The arrows highlight blurring artifacts in the frontal (blue) and posterior (red) part of the brain.

Dynamic field information was based on concurrent recording with field sensors throughout. In particular, it was used not only for spiral scanning, but also for B_0 and sensitivity mapping to enforce equal coordinates for all entries to the signal model.

Reconstructed images with an in-plane resolution of 1.3 mm showed strongly reduced blurring and aliasing artifacts and were geometrically congruent between different diffusion directions. At an echo time of only 34 ms for a b-factor of 1,000 s/mm^2, considerably higher signal amplitude at TE was available compared to single-shot EPI, where echo times below 70 ms are hard to achieve for similar imaging parameters.

The phantom study showed that incorporating recorded dynamic field information into image reconstruction diminished artifacts present in images based on nominal field evolution. Incorporation of dynamic higher-order fields made a palpable difference in removing blurring and aliasing artifacts. It was particularly effective for DWIs, which are affected by higher-order fields attributed to eddy currents induced by the diffusion gradients.

Congruence among variably diffusion-encoded images significantly improved the resolution of the mean DWIs. It also permits straightforward image combination for advanced diffusion analyses.

Compared to EPI, where static B_0 off-resonance causes pixel shifts, in spiral imaging it leads to blurring, which is visually more disturbing and corrupts quantitative evaluation even on a per-pixel basis. Effective off-resonance correction is thus crucial in deploying long spiral readouts. Still, minor residual off-resonance artifacts were observed in vivo. Slight residual blurring in the frontal and posterior part of the brain reflects error in the signal model, most likely in the B_0 map, amplified by adverse conditioning. The residual artifacts thus

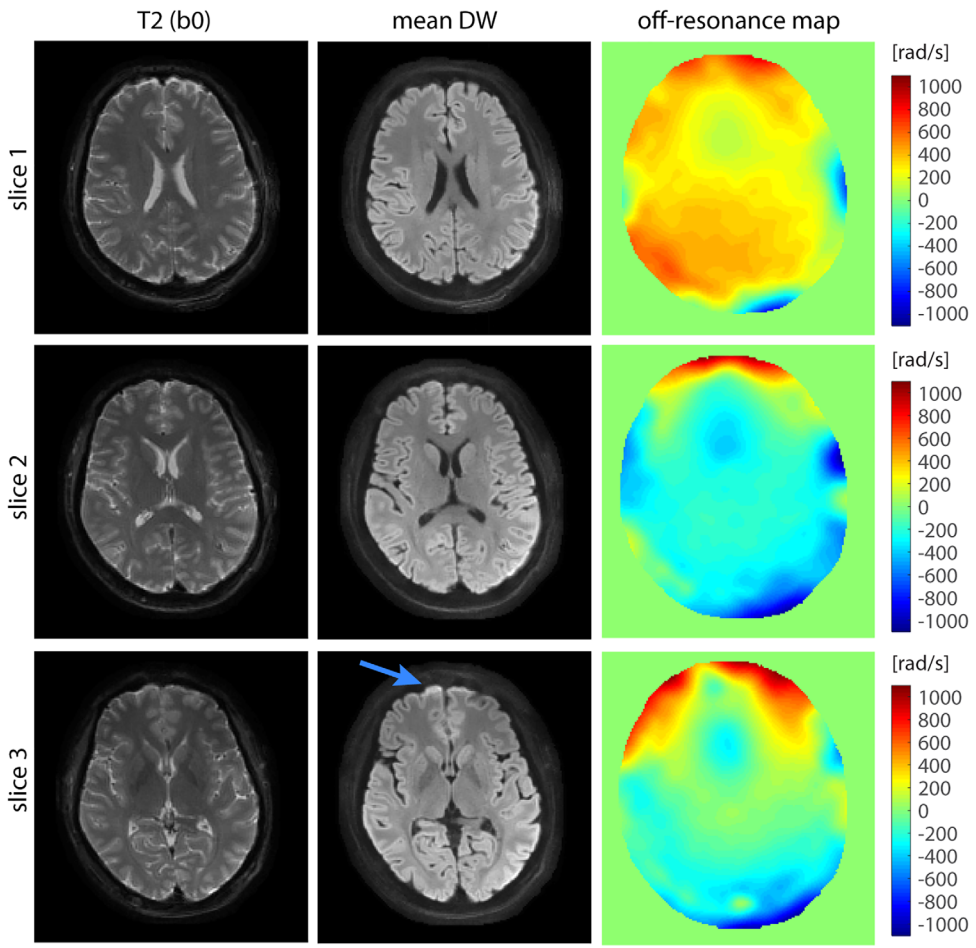

FIG. 6. In vivo single-shot spiral images in different slices. Columns (left to right): T2-weighted (b0) image, mean DW image, ΔB_0 off-resonance map. The blue arrow highlights a blurring-like artifact.

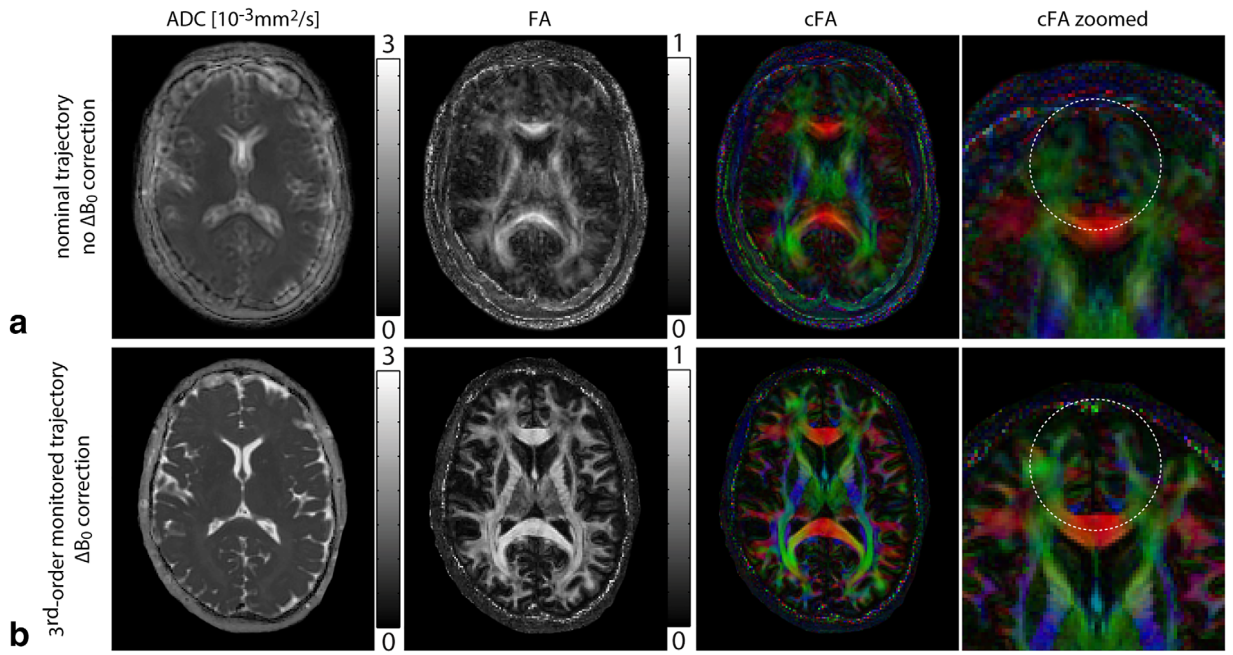

FIG. 7. DTI data reconstructed on nominal k-space trajectory (a) and using the concurrently monitored higher-order field evolution with ΔB_0 correction (b).

illustrate the limits of the correction approach, which depend on the model accuracy and the degree of encoding perturbation caused by off-resonance. These limits will be reached sooner in more-challenging ΔB_0 situations, such as in the brainstem. To render B_0 correction robust, it may then be necessary to adjust the spatial resolution, the SENSE reduction factor, or, if possible, the readout bandwidth or the FOV. At the hardware level, higher-performing gradients and associated shorter readouts will generally increase the feasibility of off-resonance correction. Moving to lower field strength, ultimately, is a natural way of reducing B_0 nonuniformity in the first place.

Notably, concurrent field monitoring also captures B_0 changes attributed to breathing motion of the chest. This was found to be critical, for example, in structural T2* imaging at high field (34). In the present work, these effects are also inherently addressed. Here, they are less critical, however, because single-shot imaging is not affected by intershot phase inconsistency, and breathing fields below 1 Hz would cause negligible blurring at the given acquisition durations. Head motion, however, will impair the validity of the static ΔB_0 maps and thus compromise reconstruction results, which may limit its utility in a clinical setup. The acquisition of the ΔB_0 maps could be further optimized, which would be particularly interesting in case of larger scan volumes. To this end, continuous field monitoring could be used in the future (35) to remove current limits that the minimum probe TR poses on the sequence TR.

To study basic feasibility, image reconstruction by model inversion was performed in the most general fashion, using straightforward matrix-vector multiplication in the iteration loops. With this implementation, reconstruction times have been in the order of several minutes per slice on a modern central processing unit (CPU). However, higher-order reconstruction can be performed substantially faster, using singular-vector separation and fast Fourier transform (36), and the first-order variant is even more efficient. The reconstruction task also lends itself readily to parallel operation on CPU or graphical processing unit cluster.

In this work, mapping of ΔB_0 relied on a conventional approach, using gradient echo images with two different echo times. Subsequent changes in B_0, up to third order in space, were automatically captured by concurrent field measurement. Alternatively, slow field changes could also be coestimated from the actual image data by finding a field map that minimizes a suitable objective function, for example, one that measures blurring (37,38). However, this approach may not fulfill the high accuracy requirements posed by the reconstruction problem, except for first-order field changes (39). Another option is to estimate field change from actual data of interest acquired with at least two different echo times (40–42). Although potentially demanding numerically, such approaches would capture slow field changes of higher spatial order than amenable with external field probes.

Finally, concurrently recorded field information in expanded signal models may be of similar use to other advanced approaches that could be used for diffusion imaging, including the joint estimation of parametric data (41–43), simultaneous multiple-slice imaging (44,45), and advanced interleaved techniques (5–7).

ACKNOWLEDGMENTS

Technical support from Philips Healthcare is gratefully acknowledged. This work was partly funded by the NCCR Neural Plasticity and Repair.

REFERENCES

1. Ahn CB, Kim JH, Cho ZH. High-speed spiral-scan echo planar NMR imaging—I. IEEE Trans Med Imaging 1986;5:2–7.
2. Block KT, Frahm J. Spiral imaging: a critical appraisal. J Magn Reson Imaging 2005;21:657–668.
3. Glover GH. Spiral imaging in fMRI. Neuroimage 2012;62:706–712.
4. Meyer CH, Hu BS, Nishimura DG, Macovski A. Fast spiral coronary artery imaging. Magn Reson Med 1992;28:202–213.
5. Liu C, Bammer R, Kim D, Moseley ME. Self-navigated interleaved spiral (SNAILS): application to high-resolution diffusion tensor imaging. Magn Reson Med 2004;52:1388–1396.
6. Karampinos DC, Van AT, Olivero WC, Georgiadis JG, Sutton BP. High-resolution diffusion tensor imaging of the human pons with a reduced field-of-view, multishot, variable-density, spiral acquisition at 3 T. Magn Reson Med 2009;62:1007–1016.
7. Chu ML, Chang HC, Chung HW, Truong TK, Bashir MR, Chen N. POCs-based reconstruction of multiplexed sensitivity encoded MRI (POCSMUSE): a general algorithm for reducing motion-related artifacts. Magn Reson Med 2015;74:1336–1348.
8. Pruessmann KP, Weiger M, Börnert P, Boesiger P. Advances in sensitivity encoding with arbitrary k-space trajectories. Magn Reson Med 2001;46:638–651.
9. Weiger M, Pruessmann KP, Osterbauer R, Börnert P, Boesiger P, Jezzard P. Sensitivity-encoded single-shot spiral imaging for reduced susceptibility artifacts in BOLD fMRI. Magn Reson Med 2002;48:860–866.
10. Heberlein K, and Hu X. Auto-calibrated parallel spiral imaging. Magn Reson Med 2006;55:619–625.
11. Heidemann RM, Griswold MA, Seiberlich N, Krüger G, Kannengiesser SA, Kiefer B, Wiggins G, Wald LL, Jakob PM. Direct parallel image reconstructions for spiral trajectories using GRAPPA. Magn Reson Med 2006;56:317–326.
12. Noll DC, Meyer CH, Pauly JM, Nishimura DG, Macovski A. A homogeneity correction method for magnetic resonance imaging with time-varying gradients. IEEE Trans Med Imaging 1991;10:629–637.
13. Sutton BP, Noll DC, Fessler JA. Fast, iterative image reconstruction for MRI in the presence of field inhomogeneities. IEEE Trans Med Imaging 2003;22:178–188.
14. Barmet C, Tsao J, Pruessmann KP. 2005. Sensitivity encoding and B_0 inhomogeneity - A simultaneous reconstruction approach. In Proceedings of the 13th Annual Meeting of ISMRM, Miami Beach, Florida, USA, 2005, p. 682.
15. Aldefeld B, Börnert P. Effects of gradient anisotropy in MRI. Magn Reson Med 1998;39:606–614.
16. Boesch C, Gruetter R, Martin E. Temporal and spatial analysis of fields generated by eddy currents in superconducting magnets: optimization of corrections and quantitative characterization of magnet/gradient systems. Magn Reson Med 1991;20:268–284.
17. Liu Q, Hughes DG, Allen PS. Quantitative characterization of the eddy current fields in a 40-cm bore superconducting magnet. Magn Reson Med 1994;31:73–76.
18. Wu Y, Chronik BA, Bowen C, Mechefske CK, Rutt BK. Gradient-induced acoustic and magnetic field fluctuations in a 4T whole-body MR imager. Magn Reson Med 2000;44:532–536.
19. Busch J, Vannesjo SJ, Barmet C, Pruessmann KP, Kozerke S. Analysis of temperature dependence of background phase errors in phase-contrast cardiovascular magnetic resonance. J Cardiovasc Magn Reson 2014;16:97.
20. Kasper L, Bollmann S, Vannesjo SJ, Gross S, Haeberlin M, Dietrich BE, Pruessmann KP. Monitoring, analysis, and correction of magnetic field fluctuations in echo planar imaging time series. Magn Reson Med 2015;74:396–409.
21. Vannesjo SJ, Haeberlin M, Kasper L, Pavan M, Wilm BJ, Barmet C, Pruessmann KP. Gradient system characterization by impulse response measurements with a dynamic field camera. Magn Reson Med 2013;69:583–593.

22. Bernstein MA, Zhou XJ, Polzin JA, King KF, Ganin A, Pelc NJ, Glover GH. Concomitant gradient terms in phase contrast MR: analysis and correction. Magn Reson Med 1998;39:300–308.
23. Bruder H, Fischer H, Reinfelder HE, Schmitt F. Image reconstruction for echo planar imaging with nonequidistant k-space sampling. Magn Reson Med 1992;23:311–323.
24. Alley MT, Glover GH, Pelc NJ. Gradient characterization using a Fourier-transform technique. Magn Reson Med 1998;39:581–587.
25. Duyn JH, Yang Y, Frank JA, van der Veen JW. Simple correction method for k-space trajectory deviations in MRI. J Magn Reson 1998; 132:150–153.
26. Mason GF, Harshbarger T, Hetherington HP, Zhang Y, Pohost GM, Twieg DB. A method to measure arbitrary k-space trajectories for rapid MR imaging. Magn Reson Med 1997;38:492–496.
27. Barmet C, De Zanche N, Pruessmann KP. Spatiotemporal magnetic field monitoring for MR. Magn Reson Med 2008;60:187–197.
28. Robison RK, Devaraj A, Pipe JG. Fast, simple gradient delay estimation for spiral MRI. Magn Reson Med 2010;63:1683–1690.
29. Tan H, Meyer CH. Estimation of k-space trajectories in spiral MRI. Magn Reson Med 2009;61:1396–1404.
30. De Zanche N, Barmet C, Nordmeyer-Massner JA, Pruessmann KP. NMR probes for measuring magnetic fields and field dynamics in MR systems. Magn Reson Med 2008;60:176–186.
31. Wilm BJ, Barmet C, Pavan M, Pruessmann KP. Higher order reconstruction for MRI in the presence of spatiotemporal field perturbations. Magn Reson Med 2011;65:1690–1701.
32. Wilm BJ, Nagy Z, Barmet C, et al. Diffusion MRI with concurrent magnetic field monitoring. Magn Reson Med 2015;74:925–933.
33. Basser PJ, Mattiello J, LeBihan D. Estimation of the effective self-diffusion tensor from the NMR spin echo. J Magn Reson B 1994;103:247–254.
34. Duerst Y, Wilm BJ, Dietrich BE, Vannesjo SJ, Barmet C, Schmid T, Brunner DO, Pruessmann KP. Real-time feedback for spatiotemporal field stabilization in MR systems. Magn Reson Med 2015;73:884–893.
35. Dietrich BE, Brunner DO, Wilm BJ, Barmet C, Pruessmann KP. Continuous magnetic field monitoring using rapid re-excitation of NMR probe sets. IEEE Trans Med Imaging 2016;35:1452–1462.
36. Wilm BJ, Barmet C, Pruessmann KP. Fast higher-order MR image reconstruction using singular-vector separation. IEEE Trans Med Imaging 2012;31:1396–1403.
37. Noll DC, Pauly JM, Meyer CH, Nishimura DG, Macovski A. Deblurring for non-2D Fourier transform magnetic resonance imaging. Magn Reson Med 1992;25:319–333.
38. Man LC, Pauly JM, Macovski A. Improved automatic off-resonance correction without a field map in spiral imaging. Magn Reson Med 1997;37:906–913.
39. Chen W, Meyer CH. Fast automatic linear off-resonance correction method for spiral imaging. Magn Reson Med 2006;56:457–462.
40. Kadah YM, Hu X. Simulated phase evolution rewinding (SPHERE): a technique for reducing B0 inhomogeneity effects in MR images. Magn Reson Med 1997;38:615–627.
41. Nayak KS, Tsai C-M, Meyer CH, Nishimura DG. Efficient off-resonance correction for spiral imaging. Magn Reson Med 2001;45: 521–524.
42. Sutton BP, Noll DC, Fessler JA. Dynamic field map estimation using a spiral-in/spiral-out acquisition. Magn Reson Med 2004;51:1194–1204.
43. Burakiewicz J, Charles-Edwards GD, Goh V, Schaeffter T. Water–fat separation in diffusion-weighted EPI using an IDEAL approach with image navigator. Magn Reson Med 2015;73:964–972.
44. Larkman DJ, Hajnal JV, Herlihy AH, Coutts GA, Young IR, Ehnholm G. Use of multicoil arrays for separation of signal from multiple slices simultaneously excited. J Magn Reson Imaging 2001;13: 313–317.
45. Feinberg DA, Setsompop K. Ultra-fast MRI of the human brain with simultaneous multi-slice imaging. J Magn Reson 2013;229:90–100.

SUPPORTING INFORMATION

Additional supporting information can be found in the online version of this article.

Video S1. In vivo DW single-shot spiral images. Comparison of image quality when using different encoding models.